Detection of passive scalar interface directly from PIV particle images in inhomogeneous turbulent flows

L. Gan

Abstract This article proposes a technique to estimate the cross-sectional scalar interface (outer boundary) in an inhomogeneous turbulent flow from a conditioned particle image velocimetry (PIV) experiment, which is suitable for medium to high Reynolds numbers. The scalar interface is estimated directly by using conditioned PIV particle images which have distinguishably high particle seeding density in the area of interest, whereas conventionally in water based experiments, scalar interface is often determined from planar laser induced fluorescence (PLIF) or equivalent dye images. By comparing quantities in the vicinity of this scalar interface, it also shows that in terms of separate turbulent and non-turbulent regions, this technique could also replace the function of PLIF images in water experiments, with slightly lower spatial resolution. At the same time, if velocity information is also required simultaneously then the cost of a separate camera-laser system can be saved. The effect of particle field inhomogeneity on the PIV accuracy can be well reduced to an insignificant level by an image local normalisation treatment. This article shows that the interfacial layer could be detected fairly accurately by enhancing the particle images by wavelet based thresholding methods. The degree of detection accuracy is quantified by synthetic particle image analyses, where a scalar interface can be artificially pre-defined. The proposed technique is tested in two water based experiments but is expected to be particularly useful in gas-phase based experiments or some combustion applications, where liquid-phase dye cannot be applied.

Keywords liquid or gas based experiments · scalar interface · velocity field · PIV

1 Introduction

Scalar interface separating the scalar marked area from the rest is often interesting to know in inhomogeneous high Reynolds number turbulent flows, for both liquid and gas phased applications. Not only does it reflect the scalar diffusion property due to turbulence mixing

L. Gan

School of Engineering and Computing Sciences, Durham University, Durham, DH1 3LE, UK
Tel.: +44 (0) 191 33 42438
Fax: +44 (0) 191 334 2408
E-mail: lian.gan@durham.ac.uk

in such flows, sometimes other interesting physical quantities can also be inferred from it, for instance the front of a flame (26). Another application of scalar interface in the field of experimental non-reacting fluid mechanics is that it has been used before as one of the ways to mark out turbulence non-turbulence interface (TNTI). TNTI is usually defined by the transitional zone between the outside irrotational region and the inside highly concentrated, fully developed turbulent region (see 12; 28; 13, for example).

In such applications, since turbulent velocity field and scalar interface are often both required, it usually needs simultaneous determination of the two. An example is the water based experimental work in (8), where the planar velocity field was captured by a standard 2D PIV system and the scalar field was obtained simultaneously by a PLIF system which was carefully synchronised to image in between the two PIV recordings. The scalar interface can be marked out by choosing a proper intensity threshold in the scalar image. A good way of picking such a threshold from a non-empirical approach in typical PLIF images is given by (25). Subsequent studies (30; 31; 32) based on this method are then conducted to address various problems near the interfacial layers of a fully developed turbulent jet.

However simultaneous measurements of velocity and scalar interface is relatively expensive. On the one hand, in the works mentioned above, an independent laser-camera system was adopted to capture the scalar field on top of a PIV system for the velocity field, but in many laboratories a second laser is often not available; on the other hand, great care is needed when aligning the two systems on the same field of view (FOV). In circumstances where the in-plane resolution of the scalar concentration is not critical, the laser for the PLIF system (a laser with a different wavelength to the PIV one) could possibly be saved, but two band-pass lens filters are still necessary for different cameras to see PIV particles and the scalar (usually a type of fluorescent dye) separately, and the effort to maximize the overlapped FOVs remains. Note that because the thickness of the laser sheet for PLIF to measure scalar concentration could be much smaller than that for PIV[1], when the PLIF laser is saved, the resolution of the concentration measurements by PLIF is also reduced to the one comparable to the PIV measurements.

Moreover, the above mentioned method is only applicable in liquid based experiments, for gas based ones, e.g. wind tunnel related works and some combustion applications, liquid phased scalar dye cannot be applied.

It also is worth mentioning that for marking TNTI only, measuring scalar field is not the only approach. Other techniques which based on velocity fields only also exist. For instance, TNTI thresholdings based on enstrophy and vorticity (in cases of planar information) have found their applications in some DNS studies (2; 4; 15; 21) and an experimental work (27). TNTI thresholding can even sometimes be inferred from velocity information, example works can be found as early as 1955 (18). The work in (1) gives a brief summary of the enstrophy and velocity thresholding criteria for TNTI and proposes a new one. These thresholding methods only require velocity information, hence are less expensive than the scalar interface method. However the choices of these threshold values are kind of empirical and dependent on different flows - they don't work in a turbulent vortex ring flow for example, since the velocity field is special. The method of scalar interface, however, is less sensitive to different flow types.

The purpose of this work is therefore for assessing the possibility of replacing PLIF/PIV fields with conditioned PIV images, in terms of measuring velocity and scalar interface

---

[1] Similarly to PIV, since the in-plane resolution of PLIF concentration measurements can reach 1 pixel, the thickness of the PLIF laser could also be set equivalently to 1 pixel or smaller, for the resolution match purpose. In other words, the concentration resolution is defined by the larger one between the in-plane and the out-of-plane resolutions.
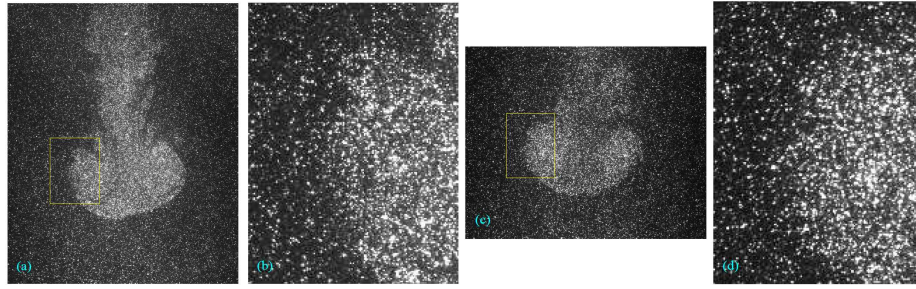
Fig. 1 Typical particle fields used to do simultaneous PIV and scalar interface estimation. In particular, it is a turbulent vortex ring at about t1= 1.40 sec (a), (b) and t2= 2.230 sec (c), (d) after the slug starts. (a), (c): the entire image showing the ring bubble and the wake structure; (b),(d) the magnified view of the selected box area near the bubble edge.

simultaneously. Two water based experiments will be used to illustrate the working principle of this technique and to discuss the related physical issues, but the nature of the technique allows it to be applicable in both liquid and gas based experiments and perhaps is particularly useful for the latter. It also is worth noting that there does exist a similar method (26) to achieve a similar objective, where interface is marked by simple spatial filtering of raw particle images, therefore it is easy to implement. However, it will be shown in § 5 that this method does not always work for the examples given.

1.1 Problem

The principle of estimating the scalar interface by a PIV image is that in any experiment in which if different regions can be distinguished by the difference of dye concentration, the dye may be replaced by PIV particles of a very high seeding concentration. The higher the concentration contrast is, the easier the passive scalar interface can be marked out by a properly chosen thresholding method (25, for example). However the challenge comes from the fact that in order for the PIV algorithm to work well, especially to give convincing vector results in the vicinity of the scalar interface, one needs sufficient concentration of particles in the background. The least seeded area limits the confidence level of the final interrogation window size, and for this reason seeding density in the background should not be too low. A fair amount of background particles will decrease the contrast and hence inevitably have a 'blurring effect' on the interfacial layer, which makes it difficult to determine.

Therefore a balance needs to be reached such that the contrast of the particle concentration across the interface is fairly noticeable, but at the same time PIV algorithm needs to function well along it. Typical images which reach such a balance are shown in figure 1. These are image samples of a turbulent vortex ring (at two time instants) of $Re \approx 20,000$ with a deliberate large seeding density inside the ring bubble structure, which is uncharacteristic for PIV-only purpose. The flow is seeded by 50μm silver coated hollow glass particles which are manufactured specially for PIV experiments. More explanations for the origin of figure 1 and the experimental configuration will be given in § 3. We can see that apart from the very highly seeded region, the background is also substantially seeded.

Such a background seeding density is reasonably sufficient for an ordinary PIV experiment. After some simple and proper image pre-processing steps, this seeding condition can easily cope with a final interrogation window size of 16×16 pix^2. One may naturally won-

der whether or not the extremely high seeding condition and the inhomogeneous seeding distribution in the vicinity of the interface shown in figure 1 will cause any detrimental effect on the PIV result. Let us defer the detailed discussion to this question to § 6, where it will be shown that a simple image local normalisation pre-processing step will minimize this potential problem.

When the velocity field can be successfully produced from these images, we would like to seek a method to estimate the scalar interfacial location by using these images, in the situations where the interfacial layer is severely interfered by background particles like it is shown in figure 1 (b) and (d). But before moving on to discuss the solution, an important issue needs to be addressed: are the highly seeded particles in the structure region really able to replace the function of a traditional scalar dye, e.g. sodium fluorescein as commonly used in water based experiments, to mark out the passive scalar interface, to a degree which is sufficient in a turbulent flow problem?

1.2 Diffusion in inhomogeneous turbulent flows

In many examples of inhomogeneous turbulent flow research, if the movement of a passive scalar marker dye is to well reflect the turbulent mixing process, then the molecular diffusion process, compared to the former, needs to be rather unimportant and negligible. In other words, the molecular diffusivity $\mathscr{D}$ of the marker scalar should be much smaller than the turbulent eddy diffusivity $\mathscr{D}_t$: $\mathscr{D}_t/\mathscr{D} \gg 1$. In a turbulent flow, the turbulent eddy diffusivity $\mathscr{D}_t$ scales with $u'l$, where u' is the characteristic turbulent fluctuating velocity and l is a proper length scale (local integral length scale). Therefore the ratio $\mathscr{D}_t/\mathscr{D}$ can be re-written, by introducing the kinematic viscosity of the fluid ν, as:

$$\frac{\mathscr{D}_t}{\mathscr{D}} \sim \frac{u'l}{\mathscr{D}} = \frac{u'l}{\nu} \times \frac{\nu}{\mathscr{D}} = Re_t \times Sc \tag{1}$$

Thus $\mathscr{D}_t/\mathscr{D} \sim Re_tSc$, where Re_t is the turbulent Reynolds number and Sc is the Schmidt number. To satisfy the condition $\mathscr{D}_t/\mathscr{D} \gg 1$, Re_tSc needs to be very large.

In an inhomogeneous turbulent flow of high Re, interface is usually a region around which strong shear takes place, so the local $Re_t \gg 1$. The fluorescent dye used to mark the flow in conventional PLIF measurements usually has a high Sc, which is in the order of 10^3. Notwithstanding the fact that in a turbulent vortex ring, the strongest shear takes place in the ring core area, the turbulence intensity in the bubble edge is also fairly significant (see 9). Moreover we now show that Sc of these particles in water is also very large.

The Sc can be worked out from the particle diffusivity $\mathscr{D}$ in water under room condition. The diffusivity $\mathscr{D}$ of particles of 50μm diameter is not well documented, but it can be estimated by the Stokes-Einstein equation:

$$\mathscr{D} = \frac{k_BT}{6\pi\mu r}, \tag{2}$$

where k_B is the Boltzmann constant, T is the absolute temperature, μ is viscosity of water and r is the radius of the spherical particle. This equation results a Sc of order 10^8. It is much larger than the Sc of typical fluorescent dye, not surprisingly, because according to equation 2, diffusivity is inversely proportional to the particle size. Therefore in the current experiment, the molecular diffusion is indeed negligible.

A simpler comment on the ratio of turbulent and molecular diffusion in the present problem is that since the particles used are neutrally buoyant and are specially designed and

manufactured to respond to the local fluid velocity instead of the diffusion motion, when the very small dye molecules (as a type of seeding) are replaced by much bigger PIV particles, in terms of marking turbulent scalar mixing, the performance of the latter is even better than the former.

To conclude, as long as it is not for an application where low Sc is specially desired, to mark out scalar boundary for turbulent mixing by very high seeding particle density is equivalent or better than to mark it by traditional large Sc dyes.

1.3 Image enhancement/denoising techniques

Having sorted out the fundamental issue of diffusion, we now propose an image enhancement technique as a potential candidate to mark out scalar interfaces in these particle images. What it is wanted is an image edge detection technique with noise reduced beforehand. Perhaps it is not difficult to notice that if we stand away from figure 1 (a) and (c), the further the picture is placed, the clearer the boundary appears to our eyes; while if we stand closer, or zoom into the picture for example (b) and (d), the boundary is harder to tell because the interference of background particles is much stronger. This is a typical resolution effect to human eyes, which inspires the wavelet based image analysis.

The key idea of it is to analyse signals by *scale*. Signals correlated with wavelets stretched to larger scales grasp the gross features while to small scales, retain the details, so that the general noise like the background in figure 1 can be reduced but the boundary can be retained. This scanning of signals is called *wavelet transform* (WT), which is a transform-domain signal processing method. Comparing to another standard transform-domain method *short time Fourier Transform* (STFT), the advantage of WT is that the window size is variable and permits a local characterisation of signals. Hence it is a multi-resolution tool which assists edge detections.

Other image denoising methods can be found as more traditional spatial-domain filtering techniques, which include median filtering, weighted median filtering (34), mean filtering (29) and Weiner filtering (14). These techniques only show strength in special cases and are not suitable for our purpose.

2 Image enhancement/denoising by wavelet thresholding

A unique prototype function used to generate the entire wavelet family is called a *mother wavelet* which is zero averaged and dilated with a scale parameter a and translated by b (6; 20; 22; 23). It can be written as:

$$\psi_{a,b}(x) = \frac{1}{\sqrt{a}} \psi\left(\frac{x-b}{a}\right), a > 0, b \in \mathbb{R} \tag{3}$$

The continuous forward wavelet transform of a 1D signal $f(x)$ at any scale a and position b yields the wavelet coefficient $\mathscr{W}f(a,b)$:

$$\mathscr{W}f(a,b) = \langle f, \psi_{a,b} \rangle = \int_{-\infty}^{+\infty} f(x) \frac{1}{\sqrt{a}} \psi^*\left(\frac{x-b}{a}\right) dx, \tag{4}$$

where $\langle , \rangle$ means inner product (convolution) and $*$ denotes the complex conjugate. One fascinating fact of WT is that the coefficient $\mathscr{W}f$ has small amplitudes if $f(x)$ is regular

over the support, while it has large amplitudes near sharp transitions such as edges in an image. This fact directly relates to edge detection and it is illustrated below.

Image denoising/enhancement is realised by thresholding the wavelet coefficients by choosing a suitable wavelet. The Daubechies wavelets are the most popular ones in the subject. Moreover in image denoising literatures, the *db*8 and *sym*8 are among the most standard ones for reporting results. For this reason, in this paper *db*8 is used. The performance assessment of different wavelets is beyond the scope of the current work and also due to the reason given below, the results are believed to be rather insensitive to different properly chosen wavelets.

In this work the *stationary wavelet transform* (SWT) and its inverse function are used. It is a redundant algorithm requiring more calculations and calling for more memory compared to a standard transform. However because of this redundancy, it generally produces better denoising quality. Another important reason behind the choice of SWT is that it gives more freedom in choosing a wavelet (20).

3 Scalar interface estimation of a turbulent vortex ring

The wavelet analysis is now applied to a flow field of a turbulent vortex ring as a test of the enhancement effect and hence the determination of the scalar interface. The turbulent vortex ring shown in figure 1 is generated in a large vortex ring generator. The detailed description of the experimental apparatus and conditions are reported in (9) in details.

The vortex ring in figure 1 has $Re = \Gamma/\nu = U_p L/2\nu = 20039 \pm 500$ and $L/D = 3.43$, where Γ is the ring circulation, D, U_p and L are the orifice diameter, the equivalent piston velocity and the slug length respectively. It is shown in (9) that vortex rings produced at these conditions are highly turbulent upon initiation.

The interface estimation technique is tested at two time instants after initiation, which are t1= 1.40 sec and t2= 2.23 sec as shown in figure 1 (a) and (c) respectively. At time t1 the ring bubble consists of a significant slug wake; at t2 some wake is shed from the ring bubble. The technique is illustrated with the image at t1.

3.1 Image enhancement

Since the lighting condition in the experiment was designed for optimising PIV purposes, when the seeding density is abnormally high, a significant fraction of the CCD pixels are saturated (i.e. reaches 255 counts in 8 bit images). To reduce the difficulty in the subsequent wavelet analysis stage, the first step is to remove the saturated pixels by convolving the image $I(x,y)$ with a Gaussian kernel of size σ_f. The σ_f scales with the characteristic particle size in the image. In the current image, it is set to 4 pixels. The image is then decomposed using SWT. The cumulative distribution function (CDF) of the wavelet coefficient magnitude $|\mathscr{W}f|$, or in abbreviation $|\lambda|$, in each decomposition level is shown in figure 2.

The number of decomposition levels required is determined by the subsequent wavelet thresholding method. The choice of this wavelet threshold $T_\mathscr{W}$ together with an appropriate thresholding method are the key steps to assist the interface determination. In this work two simple methods will be tested: the universal threshold and a level dependent threshold.
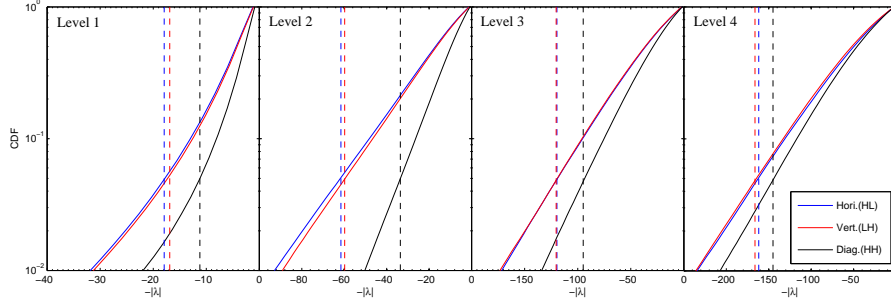
Fig. 2 The CDF of the wavelet coefficient magnitude $|\lambda|$ in each decomposition level. Only four levels are shown. A CDF value of 0.05 is indicated by the intersection of the vertical dashed lines and the distribution lines.

3.1.1 Universal threshold

The pioneering work of (7) proposes a universal threshold $T_{\mathscr{W}}^{un}$ which is proportional to the variance of the additive noise:

$$T_{\mathscr{W}}^{un} = \hat{\sigma}_{\mathscr{N}} \sqrt{2log(N)}, \tag{5}$$

where $\hat{\sigma}_{\mathscr{N}}$ is the standard deviation of the noise and N is the total number of wavelet coefficients in a given image. The estimation of the threshold in this way is also called *VisuShrink*. The noise in the image is however much more complicated than those reported in the literature and it cannot be catalogued into any standard type. The standard deviation of the noise thus is not a known quantity, but it can be estimated.

In wavelet-based method $\hat{\sigma}_{\mathscr{N}}$ is estimated from the coefficient group $HH1$[2], by the robust median estimator (7):

$$\hat{\sigma}_{\mathscr{N}} = \frac{Median(|Y_{i,j}|)}{0.6745}, Y_{i,j} \in \text{subband } HH1. \tag{6}$$

This equation is subject to some assumptions that the image does not strictly apply, but at least it gives a non-empirical estimation which is also universal. Equation 6 gives $\hat{\sigma}_{\mathscr{N}} \approx 6.92$ which from equation 5, gives $T_{\mathscr{W}}^{un} \approx 36.44$. It is well documented in the literature that the universal threshold estimated by equation 5 and 6 is usually too high and causes oversmooth. However, due to the strong non-standard noise in the image, it is found that this $T_{\mathscr{W}}^{un}$ is not sufficient to remove enough noise. Figure 3 shows the denoising effect by soft-thresholding (see 3, for the concept of soft- and hard-thresholding) of $1\times, 2\times, 3\times$ and $4\times T_{\mathscr{W}}^{un}$ on figure 1 (a), by four levels of SWT and iSWT reconstruction. The selected threshold is applied to all the coefficients, except for the final level LL4 (19).

Four levels of SWT are found to be sufficient for the purpose. Note that more levels of SWT but a low value of $T_{\mathscr{W}}^{un}$ will not lead to an effective denoising result. Referring to figure 2, in higher levels λ usually has a large magnitude, a small $T_{\mathscr{W}}^{un}$ in higher levels has a negligible proportion of coefficients to take effect on. To account for this fact, a more efficient denoising way is by a level dependent thresholding.

---

[2] Refer to (19) for the definition of HHn and the later LLn. Coefficient group (band) HH1 contains mainly noise and is highly insensitive to isolated outliers of potentially high amplitudes.
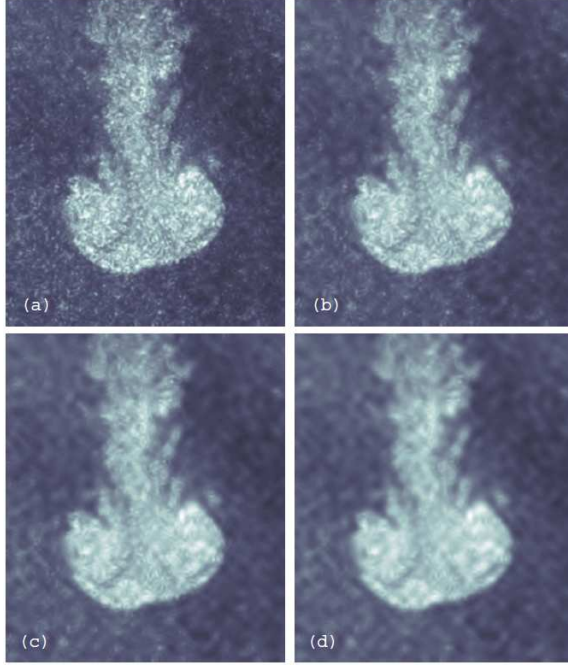
Fig. 3 Image denoised by four levels of SWT/iSWT and soft-thresholding on universal threshold values; (a)-(d) are for $1\times$ to $4\times T_{\mathcal{W}}^{un}$.

3.1.2 Level dependent threshold

An fraction value is chosen such that in each level and each subband, a number fraction of 0.05 largest magnitude coefficients λ are kept and soft-thresholded, all the smaller coefficients are zeroed; see figure 2. This way is also called *LevelShrink*, and the threshold is denoted $T_{\mathcal{W}}^{lv}$. Using this value the effect of the decomposition levels on the denoising outcomes are presented in figure 4.

The strength of the denoising effect depends on the amount of details required. It will be shown in §3.2 that the degree of smoothness in figure 3 (d) and 4 (b) is suitable for us. Note that the combination of the fraction value (0.05) and the number of decomposition levels is not unique. The current combination is chosen by optimising both computational effort and the amount of details preserved.

There are more sophisticated threshold $T_{\mathcal{W}}$ determination methods available in the image processing community; see (20) Chapter 11 for more details. The performance of these techniques is not tested here, since simple techniques introduced in this work seem to produce good enough results.

3.2 The interface determination

The central idea through the steps described in §3.1 is to enable a sensible and objective way to determine the threshold value based on image intensity counts Λ, T_Λ, to mark out the interfacial layer, which is similar to the way proposed by (25). The denoised/enhanced
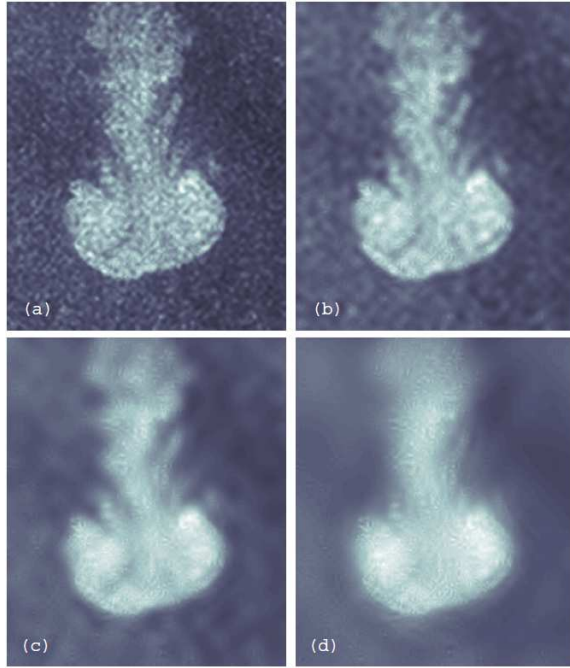
Fig. 4 Effect of number of levels of SWT and iSWT on the enhancement effect. Soft-thresholding is applied on level dependent threshold values: 95% of the small magnitude coefficients are thresholded. (a)-(d) are for level 3 to 6.

image in figure 3 (d) or figure 4 (b) are applicable to one of the two cases (the non-bimodal case) analysed in (25), but it will be shown that the T_Λ determination method generally lead to less accurate results. Therefore another way of estimating this optimal T_Λ with a better confidence level is now proposed. This is shown in figure 5.

The denoised image figure 3 (d) or figure 4 (b) has such a property that the background has low intensity Λ and the distribution of contour lines for the background Λ is relatively sparse; see figure 5 (a). Starting from small values, when a certain Λ value is reached, the contour line distribution becomes dense and converges to the desired scalar interface. In order to non-empirically estimate the T_Λ, the area of the image covered by each level of Λ, $A(\Lambda)$ normalised by the image size A_Σ, is plotted in figure 5 (b). It is easily noticed that after $\Lambda \approx 100$, $A(\Lambda)$ stays at a low level and becomes very flat. The optimal T_Λ becomes clearer if $\beta(\Lambda)$ defined by:

$$\beta(\Lambda) = \frac{1}{A_\Sigma} \frac{dA(\Lambda)}{d\Lambda} \tag{7}$$

is plotted in (c). The $\beta(\Lambda)$ represents the difference of the area covered by neighbouring Λs. The optimal T_Λ is set at the Λ value where $\beta(\Lambda)$ approaches zero for the very first time and after which $\beta(\Lambda)$ oscillates around zero at a relatively small amplitude. The difference of the $\beta(\Lambda)$ behaviour before and after the T_Λ (marked by the vertical lines in b and c) is noticeable. The choice of the T_Λ is actually rather insensitive. For instance Λ after 94 mainly affects the areas on the top region of figure 5 (a), where the wake ends; the bubble shape is not affected.
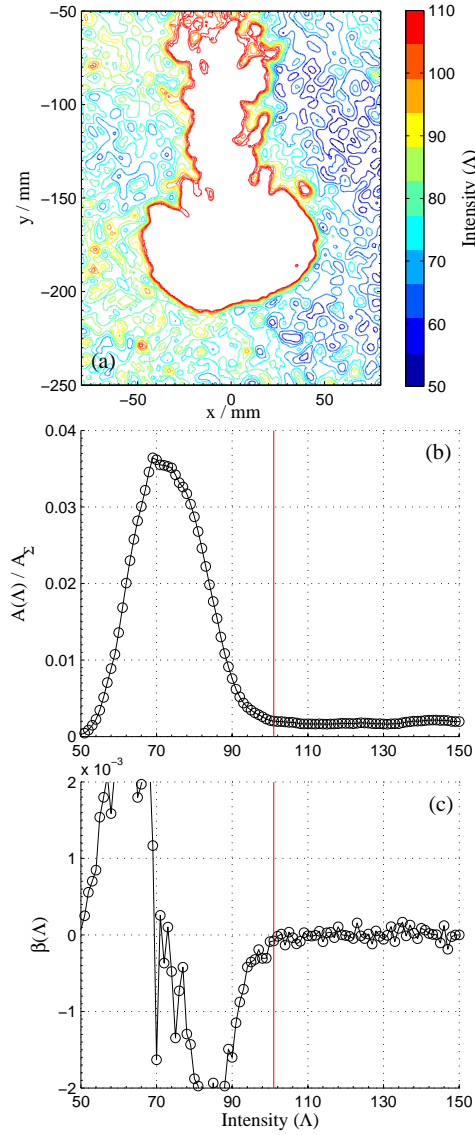
Fig. 5 The determination of the intensity threshold T_Λ to mark out the scalar interface. (a) contours of intensity Λ in figure 4 (b); (b) the area $A(\Lambda)$ covered by each intensity level Λ normalised by the area of the image A_Σ; (c) the difference of the $A(\Lambda)$ covered by neighbouring Λs, $\beta(\Lambda)$. The vertical lines in (b) and (c) indicate the chosen T_Λ.

Using this optimal T_Λ to threshold the denoised image, i.e. $\Lambda(x,y) = 0$ if $\Lambda(x,y) < T_\Lambda$, then finding the connected region of the bubble area and removing the inner holes, the interface is marked out. In some cases, to make the interface a little smoother, one level of Gaussian convolution of $\sigma_f = 5$ followed by a 5×5 median filtering can be applied before the T_Λ thresholding stage. This final smoothing treatment has a very gentle effect (since it is to the image after the denoising step), which does not alter the shape of the interface, but just
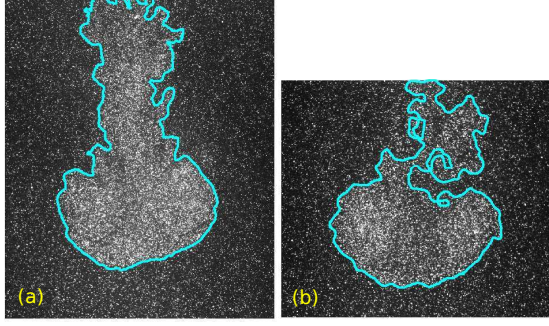
Fig. 6 The scalar interface determined by $T_{\mathscr{W}}^{ly}$ and T_Λ for t=t1 (a) and t=t2 (b); both marked on the raw particle images

smooths the interfacial line and moreover it generally only takes effect on regions where the seeding density contrast is lower, for example the wake part in figure 5 (a). The interfacial line is presented in figure 6 (a).

It must be emphasised that the central target of the wavelet thresholding technique introduced above is to degrade the noise and to make the determination of T_Λ objective. Other methods, e.g. a multi-level median filtering process which is suitable for removing *salt and pepper noise* causes a strong artificial pattern and leads to a difficult determination of T_Λ.

The wavelet denoising technique discussed in §3.1 and the T_Λ determination are applied to the same turbulent vortex ring but at a later stage t2= 2.23 sec. Due to strong detrainment of the fluid from the ring bubble and entrainment of the ambient fluid into it (9), the contrast of the seeding density inside and outside the bubble is lower, i.e. the interface is less obvious than the ring at t1. It is shown that under such a 'difficult' situation, the proposed technique is still capable of capturing the bubble.

For this image, the optimal $T_{\mathscr{W}}^{un}$ is still found to be $4\times$ that estimated by equation 5 and 6, despite the different seeding contrast condition. For the LevelShrink, it is found that instead of 0.05, a fraction of 0.01 needs to be applied to remove even more smaller magnitude wavelet coefficients in order to obtain the optimal $T_{\mathscr{W}}^{ly}$. After the wavelet threshold $T_{\mathscr{W}}$ is found, T_Λ is obtained in the same way and the numerical value is surprisingly closed to the one for t1, which is $T_\Lambda = 96$ (at t1, $T_\Lambda = 101$). The determined interface at t2 is given in figure 6 (b).

The wavelet threshold $T_{\mathscr{W}}$ determined by the two methods lead to almost identical interfacial shapes. The only disagreement takes place in the wake part, where the seeding contrast is low and the interface of the two regions are less definite; figure not shown.

4 Uncertainty estimation

In this section an uncertainty quantification of the proposed technique is applied using synthetic particle images. The most important advantage of synthetic image analysis is that one can define a 'true' scalar interface, against which the results can be benchmarked.
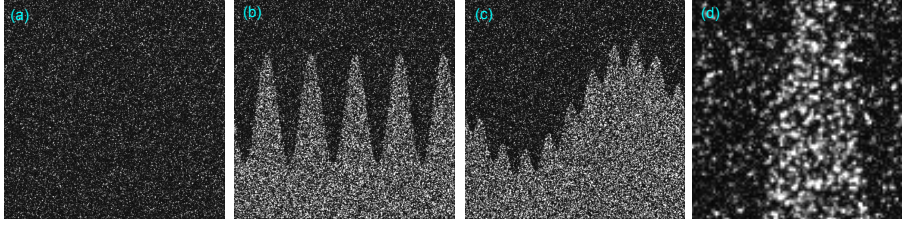
Fig. 7 Synthetic particle image analyses of the proposed scalar interface detection method. (a) the background image 512×512 pix^2; (b) superposition of particle images to generate higher density inside the pre-defined primary interfacial structure with $\Lambda_i/\Lambda_o \approx 2$, wave number $k_1 = 5$; (c) superposition of a secondary structure of secondary wave number $k_2 = 10$ onto the primary structure $k_1 = 1$; (d) a zoomed-in view of (b).

4.1 Synthetic particle image generation

The synthetic particle images are generated by the following steps. First, a homogeneously and randomly distributed particle field is generated as the background with Gaussian distributed particle sizes (typically appear as 3-5 pixel in diameter) and intensities; see figure 7 (a). Some white and non-white noise are also added, such that the PDF of the pixel intensity is similar to that of the real PIV background particle images. The particle number density is controlled such that inside a 16×16 pix^2 window, there are about 15 particles to ensure PIV accuracy for real-world situations.

Next, a set of sinusoidal curves are used as pre-defined interfaces, with the primary wave number k_1 varies from 1 to 5, while keeping the amplitude constant at $A_1 \equiv 128$ pixels. The intensity inside the interface is controlled by superimposing a number of background images but with particles whose centroids locating outside of the pre-defined interface removed. Figure 7 (b) shows the particular case at $k_1 = 5$ and the averaged pixel intensity ratio of the inside to the outside of the defined interface $\Lambda_i/\Lambda_o \approx 2$. A zoomed in view in the vicinity of the interface is shown in (d). Note that the averaged pixel intensity ratio is utilised to quantify the particle density ratios inside and outside the region of interest. This is because in real experiments, when particles are highly overlapped, it is not possible to quantify the NPPP (Number of Particles Per Pixel) value to a good accuracy and Λ_i/Λ_o is the easiest accessible quantity. However, since these are synthetic particle images, NPPP values are preset. As a guide, the ratio $NPPP_i/NPPP_o$ varies from 2 to 11 in a step of unity approximately (superposition effect). Bearing in mind that this is a 2D NPPP, not volumetric one. Some secondary structures are also used to test the uncertainty. The secondary structures are also sinusoidal waves but are superimposed onto the primary structure of $k_1 = 1$; see (c). Three secondary structures are tested with the wave number (k_2) and the amplitude (A_2) pairing as $[k_2, A_2] = [10, (1/4)A_1], [20, (1/8)A_1], [30, (1/12)A_1]$, in order to mimic a range of small structures in some real turbulent flows. These correspond to the absolute wavelength and amplitude pair in pixels as: $(51.2, 32), (25.6, 16), (17, 10.7)$.

4.2 Error quantification

The deviation quantification of the detected interface to the pre-defined one is now performed as k_1, k_2 and Λ_i/Λ_o are varied. Only the results from the universal thresholding
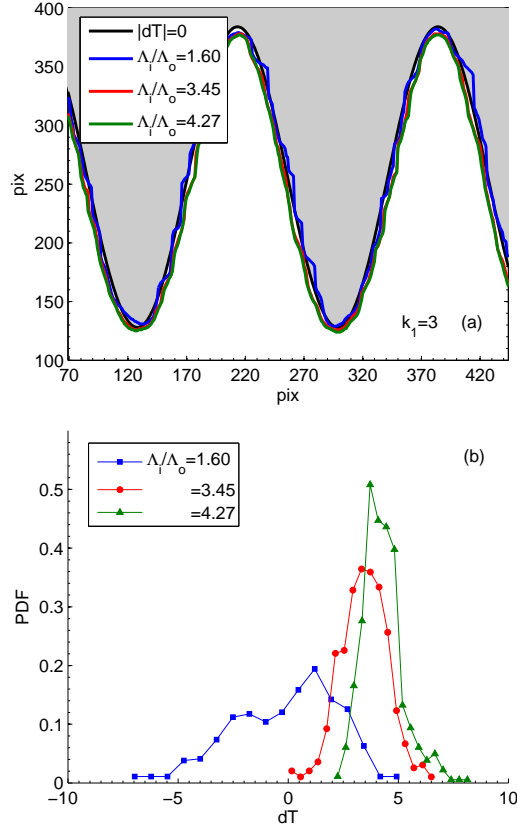
Fig. 8 The deviation dT (in pixel) as a function of $\Lambda_i/\Lambda_o \approx 2$ at $k_1 = 3$ ($k_2 = 0$). (a) a visualisation of the detected interface; where $|dT| = 0$ denotes the pre-defined interface and the shaded zone represents the scalar zone. (b) the PDF of dT.

method (§3.1.1) will be presented. Figure 8 gives an example of the detection quality at $k_1 = 3$ without secondary structures. The amount of deviation is in the unit of pixel and is denoted as dT, where dT > 0 means the detected interface pixel location is outside of the scalar marked (higher intensity) zone and dT < 0 inside. It is clear from (a) that for all the intensity ratios tested, the proposed method manages to capture the sinusoidal shape, the larger the Λ_i/Λ_o, the smoother the detected interface. From the PDF in (b), it shows that when Λ_i/Λ_o is low, the mean detected interfacial location agrees with the pre-defined one better with the mean dT ≈ 0. But it does not mean that the quality of the detection is better for low Λ_i/Λ_o because it has a larger rms value (a wider distribution). When Λ_i/Λ_o increases, the detected interface becomes *systematically* outside of the pre-defined one with the mean dT larger but the rms smaller.

Figure 9 (a) shows the magnitudes of the deviation $|dT|$ as a function of the intensity ratio Λ_i/Λ_o. Not surprisingly, when Λ_i/Λ_o is low, $|dT|$ is larger, since the distinction on the two sides of the interface is not clear enough at some locations. When this intensity ratio rises to around 2, $|dT|$ minimises at 2-3 pixels, while if the intensity ratio goes higher,
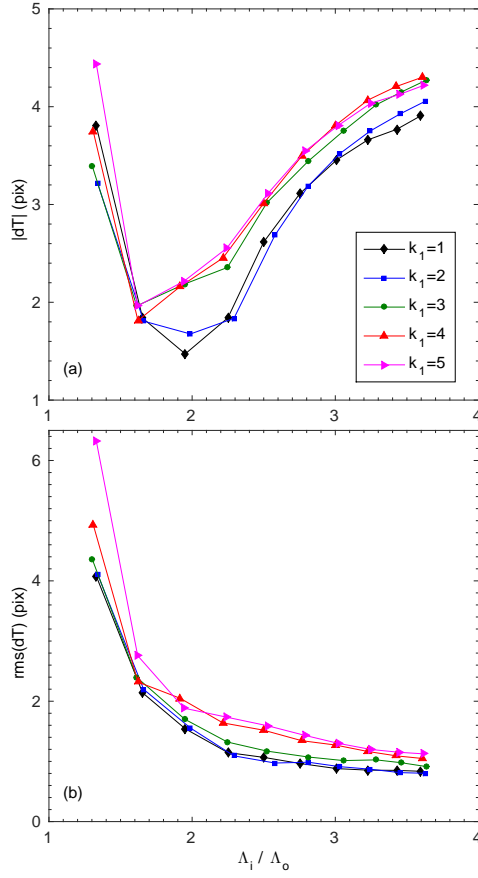
Fig. 9 The deviation magnitude |dT| and the rms dT as functions of the intensity ratio of the inside to the outside of the scalar interface Λ_i/Λ_o, for the primary wave structure $k_1 = 1$ to $k_1 = 5$. (a) the magnitude, or the absolute deviation |dT|; (b) the rms dT. The corresponding 2D NPPP ratio is approximately from 2 to 11 in a step of unity.

|dT| increases again. This is because the systematic error mentioned above gets larger; see figure 8 (b). Overall, the largest deviation is within $\sim$4 pixels, which is about one particle diameter. Figure 9 (b) shows the behaviour of the rms dT, which effectively means how smooth the detected interface is with respect to the pre-defined one. The rms dT is a monotonic decreasing function of the intensity ratio, which is also in agreement with figure 8. Therefore for the vortex ring image case in figure 1 (a), where $\Lambda_i/\Lambda_o \approx 2$, both the averaged deviation and its rms should be around 2 pixels. Moreover, the behaviours of |dT| and rms dT are shown to be rather insensitive to the wave numbers.

Finally when secondary structures are added on to the primary one ($k_1 = 1$ only), the results are given in figure 10. At $\Lambda_i/\Lambda_o \approx 2.25$, the detected quality is shown in (a) to (c) for $k_2 = 10, 20, 30$ respectively. It indicates that when the secondary structures become as small as 17 pixels and 10.7 pixels for wavelength and amplitude respectively, the detected deviation still remains within about 2 pixels. For instance, it still captures the 'teeth' in (c).
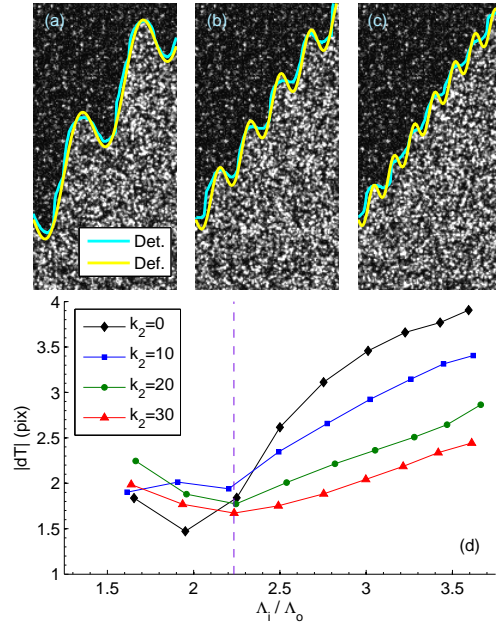
Fig. 10 The deviation of the detected interface on the secondary structures superimposed on the primary structure $k_1 = 1$. (a) $k_2 = 10$, (b) $k_2 = 20$ (c) $k_2 = 30$; 'Det.' denotes the detected interface and 'Def.' the pre-defined interface. (d) the quantification of the deviation magnitude $|dT|$ as a function of the intensity ratio Λ_i/Λ_o; the vertical dashed line marks the example ratio used in (a) to (c). The $k_2 = 0$ case (no secondary structure) is also plotted for reference purposes.

Similarly to figure 9, when the intensity ratio goes high, the magnitude of the deviation increases. Although the absolute deviation still is smaller than one particle size ($\sim$4 pixels), in terms of the relative deviation to the wave amplitude, this $|dT|$ becomes important. This means that the teeth are smoothed out. The absolute $|dT|$ is also not a strong function of k_2.

Again as the intensity ratio Λ_i/Λ_o increases, the deviation dT will always become systematic, which is always slightly outside of the defined interface. Such a systematic overestimation can be reduced by choosing a slightly higher intensity threshold than the non-empirically determined one in figure 5 (c), to 'shrink' the detected interface in-ward towards the scalar marked region.

The generation of the background particle field figure 7 (a) follows the optimal condition for PIV purpose, i.e. the averaged particle size ≈ 4 pix and $NPPP_o = 0.057$. To get a quick idea about the effect of these two parameters, the case $k_2 = 30$, which has the smallest wavelength, is used as a benchmark to assess the two parameters separately. The full assessment of the combined effect is left for future studies.

Figure 11 (a) and (b) show the effect of varying particle densities with fixed particle size. The four $NPPP_o$ correspond to 3.7, 7.3, 11, 15 and 29.3 particles in a 16 pixel window respectively. The plotted data start at a Λ_i/Λ_o value below which no convincing interface is detected. (a) also shows that $|dT|$ generally behaves accordingly to Λ_i/Λ_o instead of the $NPPP_i/NPPP_o$. Not surprisingly, a very low $NPPP_o$ value yields a very high $|dT|$, due to insufficient particles along the interface. Such a low background particle density does not generally give a good PIV signal-noise ratio anyway. For other $NPPP_o$, the detection performance is not a strong function of $NPPP$ or Λ ratio - $|dT|$ is within one particle size.
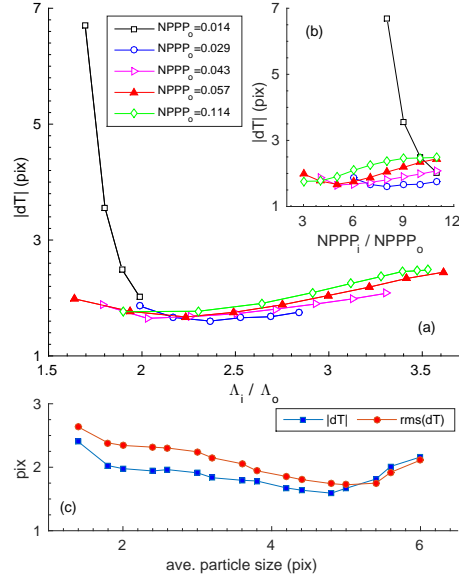
Fig. 11 Testing the effects of particle density and size using the $k_2 = 30$ case as the benchmark. (a) The deviation magnitude $|dT|$ as a function of the intensity ratio Λ_i/Λ_o for various background particle densities; (b) $|dT|$ as a function of NPPP ratios (c) $|dT|$ and rms(dT) as a function particle size (measured at 1% of the peak intensity).

Figure 11 (c) illustrates the effect of particle size while keeping the $NPPP_o$ fixed at 0.057 and $\Lambda_i/\Lambda_o = 2.23$ or $NPPP_i/NPPP_o = 5$. It shows that across the entire testing range, which is commonly adopted for PIV purpose, varying particle size does not have a significant impact on the accuracy. The overall error is also within 3 pixels, with the minimum at about 5 pixel particle size.

5 Comparison to other methods

The work (26) mentioned in § 1 achieves a similar goal by low-pass filtering the raw image with a kernel size comparable to the final PIV interrogation window. This method generally works well for interface of large wavelengths. Figure 12 (a) tests this method on synthetic images. It shows that the deviation magnitude $|dT|$ is comparable to the current proposed method. However, the method in (26) does not yield a good rms dT result. This means that it only captures the low wave number k_1 but not the teeth k_2. It is not a surprising result since a large filtering kernel and the subsequent threshold setting principle leads to a larger uncertainty for capturing small features on the interface. Furthermore, this method does not always work in real experimenal images given. In figure 12 (b), this method is presented together with the PDF of the pixel intensity counts for the raw and the denoised image at vortex ring t2. One may notice that the method in (26) does not apply since no distinguishable second peak can be identified.

When applying to the denoised image, figure 12 (c) reveals a similar behaviour as it is in (25), where the threshold value was suggested to be the turning point connecting the two linear parts. To determine the location of this point is relatively subjective, since it is
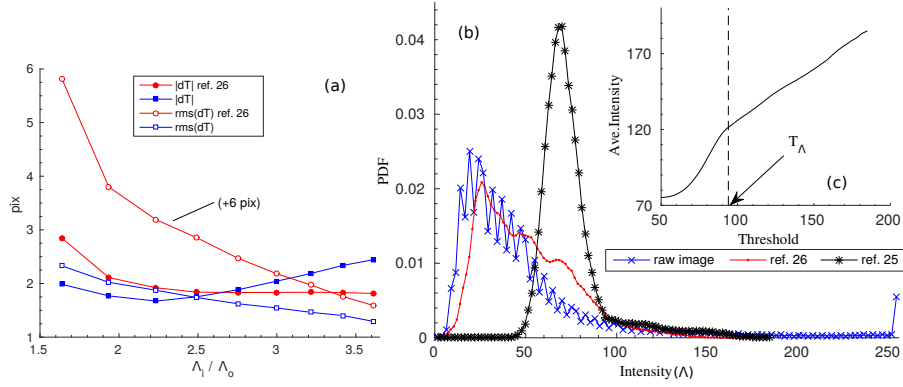
Fig. 12 Comparison to other proposed methods for the ring image at t2. (a): compare to the method in ref. (26) for synthetic images case $k_1 = 1, k_2 = 30$. The rms(dT) ref. (26) line is shifted downwards for 6 pixels for clearer interpretation purpose. (b): PDF of pixel intensities for the raw image figure 1(c), method in ref. (26) and method in ref. (25). (c): averaged intensity as a function of the threshold level, derived from (b) line ref. (25); see ref. (25) Fig. 8; T_Λ: the threshold determined by the current proposed method; see figure 5.

not sharp. By estimation, it is roughly 5-10 Λ lower than the one determined by the current proposed method, which leads to a slightly more expanded ring bubble interface ($\sim$ 4-5 pixels with some areas closed to 10 pixel). This 'turning-point' method does not work for the raw particles images at all.

6 The influence of seeding inhomogeneity on the PIV results

In §1.1 a concern was left about whether the seeding density inhomogeneity across the scalar interface will have any significant detrimental effect on the PIV results. In particular, only when interrogation windows which are across the interface, the cross-correlated velocity results will have a non-trivial bias towards the more densely seeded side. This bias is the additional error $\Delta \varepsilon$ on top of the intrinsic error ε of a PIV experiment under normal seeding conditions. For interrogation windows that do not have intersection with the interface, particles are evenly distributed inside and $\Delta \varepsilon = 0$.

The degree of the particle seeding inhomogeneity can be remarkably reduced by an image local normalisation step, equation 8. In the vortex ring example the normalisation is done after the intensity of the saturated pixels being brought down.

$$\widetilde{I}_n(x,y) = \frac{\widetilde{I}(x,y) - m_{\widetilde{I}}(x,y)}{\sigma_{\widetilde{I}}(x,y)}, \tag{8}$$

where $m(x,y)$ and $\sigma(x,y)$ are the local mean and standard deviation of the image, which are estimated by locally spatial smoothing by Gaussian kernels of σ_1 and σ_2 (standard deviation) respectively. Depending on the image condition, for our case they are set as $\sigma_1 = \sigma_2 = 4$ pixels. After the local normalisation, the seeding density condition across the estimated interfaces for time t1 and t2 is shown in figure 13, in the vicinity of the windward surface where the seeding density contrast was the highest in the raw images. The particle seeding inhomogeneity in an interrogation window across the interface is no longer very severe.
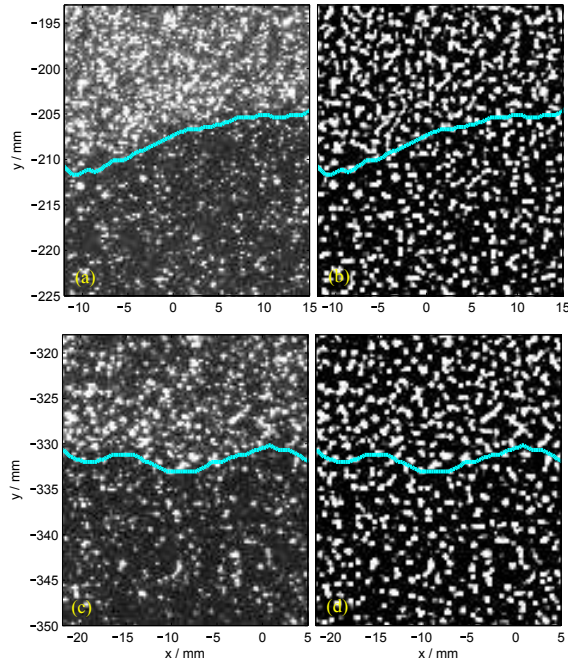
Fig. 13 The degree of particle inhomogeneity across the estimated scalar interface near the wind-ward bubble surfaces. (a), (b) t1; (c), (d) t2. (a), (c) interface marked on the raw images; (b), (d) interface marked on the locally normalised images.

The relative seeding density difference across the interface after local normalisation can be estimated by the NPPP ratio, in windows of 50×50 pixel^2 closed to the interface. The ratio of NPPP is typically $1.1 - 1.2$ for both t1 and t2.

It must be stressed that it is crucial to have sufficient particles seeded in the background so that after image local normalisation, the inhomogeneity can be made insignificant. This is for the sake of PIV accuracy since usually there is a local shear region in the vicinity of a scalar interface. Zero background particle condition would almost certainly bias the local velocity determination towards the seeded regions (one side of the shear region).

7 Some physical quantities near the vortex ring scalar interface

Let us now have a look at the property of the scalar interface in relation with local velocities. Figure 14 (a) and (c) show the instantaneous velocity field processed from particle fields at t1 and t1+PIV Δt, t2 and t2+PIV Δt, and the corresponding interfacial layer movement over the PIV Δt. The plotted vector fields are from 16×16 pixel window size and 50% overlap. The agreement of the vector direction/magnitude and the interface movement is clear.

The scalar interface in vortex rings usually represents the vortex ring bubble. To see the relation between the two, one needs to be in a frame of reference which matches the bubble translational velocity (celerity, see 9; 10). Figure 14 (b) and (d) show the vorticity and the velocity fields in the moving frame of reference (note that the vorticity is not affected by changing between inertial frames of reference). The velocity of the ring bubble is estimated
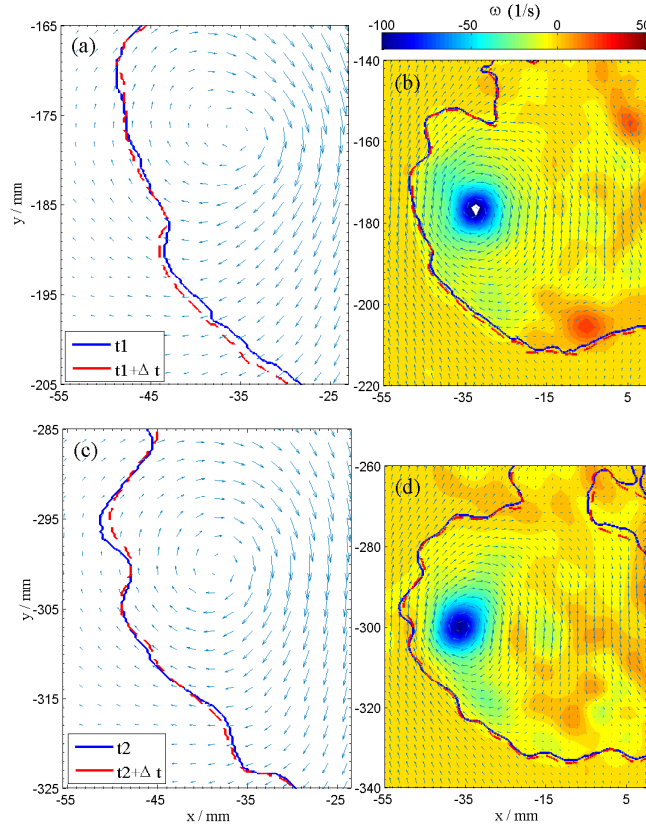
Fig. 14 Instantaneous velocity field processed by particle fields at time t and t+PIVΔt, and the corresponding interface movement over the time Δt. (a) and (b) for t1 and t1+Δt; (c) and (d) for t2 and t2+Δt. (b) and (d): vorticity field and velocity vectors in the moving frame of reference at the ring translational velocity.

by the celerity of the cores, which is further calculated by the change of locations of the two core centroids (b and d only show one core). The history of the bubble celerity of this particular ring is shown in figure 15. The two time instants t1 and t2 are marked.

The detailed way of calculating celerity can be found in (9). Due to strong turbulence and the uncertainty in locating the centroids of vortex cores, the instantaneous celerity u_t of a single ring is very unsteady. A more reasonable celerity is obtained by denoising u_t. Celerity $u_t \cdot d$ is the denoised signal of u_t by four levels of 1D Discrete WT (19) with db8 wavelet. The robustness of multi-resolution wavelet analysis is again proved: it tracks the general trend and erases the small details. Both u_t and $u_t \cdot d$ obey the trend predicted by the corrected similarity theory where celerity $\sim (t - t_o)^{\alpha}$, and $\alpha = -0.77$ (see 11, for more details). The t1 and t2 are chosen when $u_t(t1, t2) \approx u_t \cdot d(t1, t2)$.

The relation of the local velocities in the moving reference frame and the interface can be better seen when the projected streamlines are calculated based on the 2D velocities. Streamlines are constructed by using the following relations:

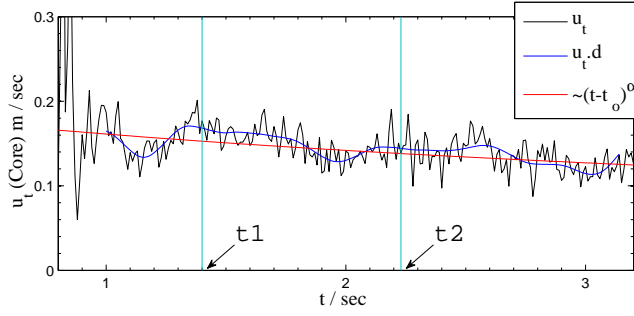$$\frac{dx}{d\tau} = u(x, y, t) \quad \frac{dy}{d\tau} = v(x, y, t), \tag{9}$$

Fig. 15 Vortex ring bubble translational velocity: celerity, calculated based on the vortex ring core positions. u_t: the instantaneous celerity; $u_t.d$ denoised u_t using 1D Discrete WT; $\sim (t - t_o)^\alpha$: the trend of u_t based on the corrected similarity theory. t1=1.40 sec and t2=2.23 sec.

where τ is a sufficiently small artificial time. The instantaneous turbulent vortex ring is highly three-dimensional, the constructed streamlines are thus projected ones. Figure 16 (a) and (c) show the interface and the streamlines starting at the stagnation points. Note that due to the existence of a small vorticity blob at $(x, y) \approx (-5, -205)$mm (see figure 14 b), there are two stagnation points in (a). In both (a) and (c) the stagnation streamline on the *lhs* rolls into the core region while the one on the *rhs* goes to the wake. It must be stressed that the interface does not necessarily collapse on top of the stagnation streamlines due to a number of reasons: the spatial resolution of PIV not being sufficient; three dimensionality; deformation of the bubble (the representation of bubble celerity by the core celerity is only an estimation, which influences the true stagnation point location). In figure 16 (b) (d), some other streamlines starting from the far field are also shown, together with the vorticity and the velocity field.

In order to see the relation between the scalar interface determined by this technique and TNTI, figure 17 is presented from the instantaneous and the ensemble information at t1 and t2. Vortex rings have a fundamental difference to jets in terms of streamwise velocity distribution, that is, due to the existence of the vortex core and the Biot-Savart law, the velocity profile across the ring centre is far from a Gaussian. This means that new velocity and length scales need to be defined specifically for vortex ring flows alone if velocity criterion is used to define TNTI. Subject to proper scale definitions, the current scalar interface shows that azimuthal vorticity ω_θ outside the interface does converge to zero quickly from about 10% of the core vorticity; see (a). In (a), R_c is the ring radius based on core locations and u_c is the ring bubble centreline streamwise velocity. Reynolds normal stresses near the interface are shown in (b). Reynolds stresses are obtained from (9), in the similarity coordinates. After the distance between the bubble interface and the core location is transformed by the similarity theory (see 9, for details), the smallest radial interface location is marked as r_i(min) in (b). Note that r_i is different for different 2D cores (left or right) at different times (see a), but at interface the magnitude is well below 5% of the core stresses.

8 Interface of a near-field jet

The scalar interface estimation method is now tested on a near-field jet. A simple turbulent jet experiment is conducted in a large water channel, which has a working section of 900×500 mm. A simple sketch of the experiment is presented in figure 18. This experi-
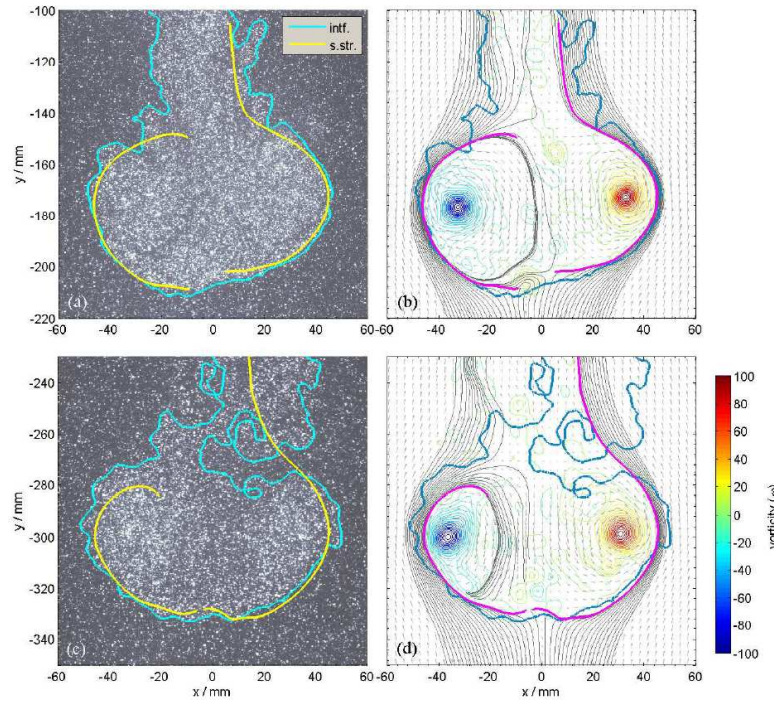
Fig. 16 Streamlines in the moving frame of reference. (a) (c) the estimated scalar interface and the stagnation streamlines drawn on the raw particle field; (b) and (d) drawn on the vorticity and velocity field, together with additional streamlines starting from the far field. intf: interfacial line; s.str: stagnation streamline.

ment was a part of a project in which stereoscopic(stereo-) PIV was used to obtain two-dimensional three-component (2D3C) velocity information in the x-y plane of a jet, cutting the nozzle exit diameter. In order to test the technique proposed in this work, only the particle images from one camera is used as the scalar field recording images, as if a 2D experiment but with a large viewing angle.

The jet nozzle is made of a perspex tube of inner diameter $D_j = \varnothing 35$mm, 3mm thick and about 400mm long. The nozzle is fixed in position by two clamp holders (not shown). The mouth of the nozzle is sharpened to about $10°$ and is painted black. A honeycomb cylindrical-shaped block is fixed at about 180mm away from the nozzle exit by a shaft and four screws as shown. The jet is generated by an inline pump system. The power of the pump is constant but the jet flow rate can be adjusted by a by-pass gate valve. The gate valve is opened at a degree which produces an average streamwise velocity of $U_j = 0.30m/s$ at the jet exit, which converts to a $Re = D_j U_j / v \approx 10500$. The 2D3C near-field velocity distribution in the x-y plane is gathered by a stereo-PIV system which consists of two cameras of 1024×1024 CCD size. The camera viewing angle is $45°$. Two prisms are also used to further reduce the distortion effect. The sheet thickness is set at about 3-4mm.

The channel is normally seeded by 10μm silver coated hollow glass particles for ordinary PIV purpose. In order to test the method, a bucket is placed inside the water channel at far upstream and serves as a reservoir for water with distinguishably higher seeding density. The bucket is made of PVC, so when the jet is running and the water in the bucket is consumed, the bucket floats up. The consumption pipe going into the bucket is fixed in-
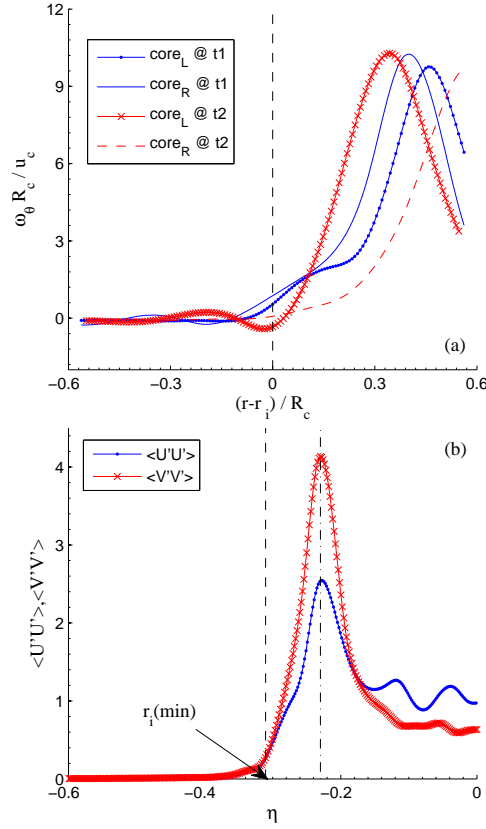
Fig. 17 Quantities near the interface of the ring bubble along the maximum ring diameter location at t1 and t2. (a) normalized vorticity ω_θ; (b) normal Reynolds stresses; $r_i\,(min)$: minimum interface location; the horizontal axis η, is the dimensionless r.

dependently to the bucket, so that when the bucket floats, the relative head between the consumption pipe inlet and the nozzle exit will not be changed and the flow rate maintains constant. In this arrangement, before the bucket empties, in principle there is no change of the water level in the channel.

The PIV sampling rate is set to 100Hz and the PIVΔt to 1ms. The calibration and the vector processing are subsequently realised by LaVision Davis 7.2. The final pass of the cross-correlation is set as 16×16 pixel interrogation window size and 50% overlap. After image dewarping and reconstruction, it gives a spatial resolution of 1.75mm based on interrogation window size. The interface is determined in the raw images first before applying image dewarping for perspective corrections. It is because the wavelet algorithm is more efficient in dealing with standard sized images, in this case 2^{10}. A typical raw image from camera 1 is given in figure 19 (a).

Interfacial lines are determined by following the two thresholding methods suggested in §3.1.1 and §3.1.2. In particular, in VisuShrink $T_\mathscr{W} = 4 \times T_\mathscr{W}^{un}$ (see equation 5 and 6) and in LevelShrink the fraction of large magnitude λ to keep is 0.15. Subsequently the T_λ is determined by the method proposed in §3.2. A distinguishable threshold value as it shown in figure 5 can be easily pinned down. It is necessary to point out that when the method
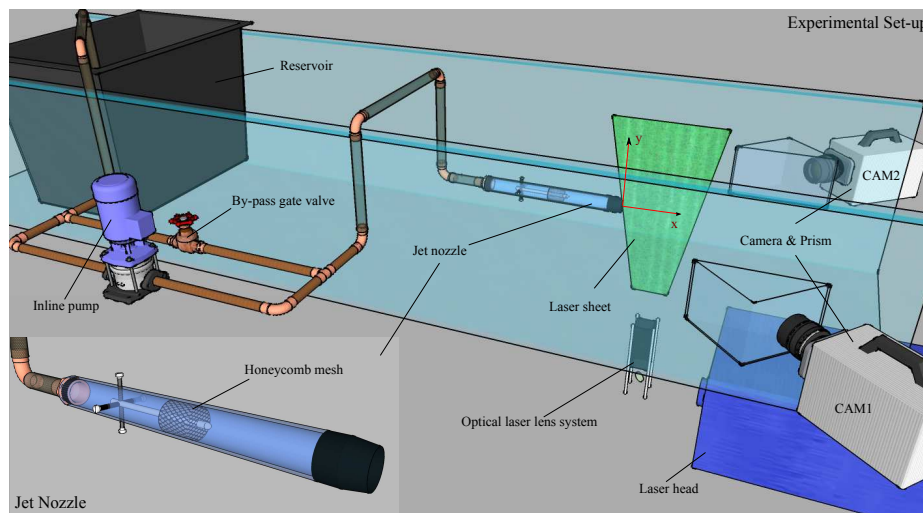
Fig. 18 The turbulent jet experiment set-up showing the jet mechanism and the PIV set-up. A stereo-PIV arrangement was adopted to study the 2D3C velocity distribution in x-y plane. The sketch is not to scale.
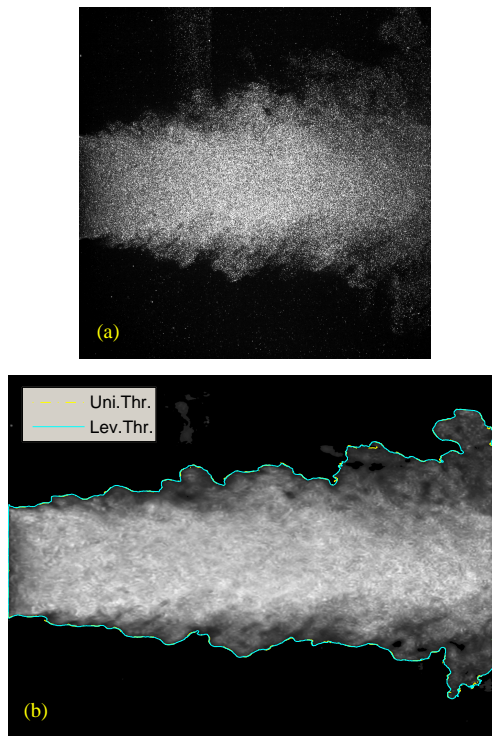

Fig. 19 The particle image in camera 1 and the estimated scalar interface. (a) the raw particle image; (b) the dewarped and enhanced particle image with interfaces by the two thresholding methods.

proposed in (25) is applied to the denoised image of this jet, a similar bi-linear behaviour to figure 12 (c) is also observed. Nevertheless the turning point failed to function because the corresponding T_Λ is way too low.

The enhanced/denoised image and the interfacial lines are then dewarped according to the method proposed in (33), The dewarped image is reconstructed by linear-interpolation. Note that for our purpose, more accurate interpolation schemes like Whittaker reconstruction are not necessary. The dewarped image is shown in figure 19 (b), together with the interfacial lines estimated by the two methods which nearly exactly collapse. It is worth emphasising that unlike the vortex ring, because the flow/seeding condition is stationary, any parameter set to optimise the interface determination remains optimal during the entire time range of the experiment.

After image local normalisation by equation 8, the inhomogeneity of the particle seeding condition across the interface is reduced,which facilitates the PIV processing in the vicinity of the interface. The typical NPPP ratio of inside and outside the interface is about 1.2.

Since the scalar interface was used to mark TNTI before (32), here comparisons are made to the velocity criterion(1; 17), in which the threshold to determine TNTI is $U/U_o = 0.03$. Figure 20 (a) illustrates the two TNTI marked on an instantaneous vorticity field. It shows that at near field the two interfaces are similar in shape and position. The interface based on the velocity criterion exhibits some abrupt jumps, which is in agreement with the findings in (1). Also plotted in this figure (b) is the intensity distribution across the interface at several downstream distances. This intensity Λ is the value obtained after the image denoising process and therefore is not the raw pixel intensity captured by the camera. It reflects the interfacial 'expansion' clearly: from a sharp step change of intensity near the nozzle exit to a more spread near-Gaussian distribution further away. More specifically, the blob outside the main stream at $x = 2D_j$ agrees with the difference between the scalar and velocity interface at the same location in (a). This shows that potentially this technique may be used to measure the scalar concentration after some proper calibration process. Figure 20 (c) shows a detailed true interfacial lines (not the envelop) on top of the instantaneous vorticity field of (a). The intensity threshold T_Λ (see § 3.2) also detects some holes inside the outer interfacial lines, with two of which labelled in (c). These holes are 'intensity holes'. Whether these intensity holes are associated with the 'turbulence holes' cannot be assessed using the current PIV setup, since the third component of the velocity is not measured.

Finally comparisons are made for the conditional averaged profiles of velocity, vorticity, Reynolds shear stress and intensity in the vicinity of the two TNTI criteria at $x = 3.5D_j$; see figure 21. These conditional averaged profiles are generated after ensemble averaging of 1000 realisations. Similarly to the velocity criterion, the detected interface from the proposed method also locates at the rising edge of all the three quantities. Some features are also in consistent with the comparisons made in (1). For instance, the velocity criterion yields a higher and sharper vorticity peak just inside the TNTI than that from the scalar interface. The intensity (Λ, after the denoising step) profile also shows a clear interfacial feature with a jump. Bear in mind that the test location is at near field, which is before the jet becomes fully self similar.

9 Discussion and conclusion

This article proposes a technique to detect scalar interface directly from raw PIV particle images so that both scalar interface (potentially concentration as well) and velocity field can be obtained simultaneously at a lower cost. The technique is tested on two water based
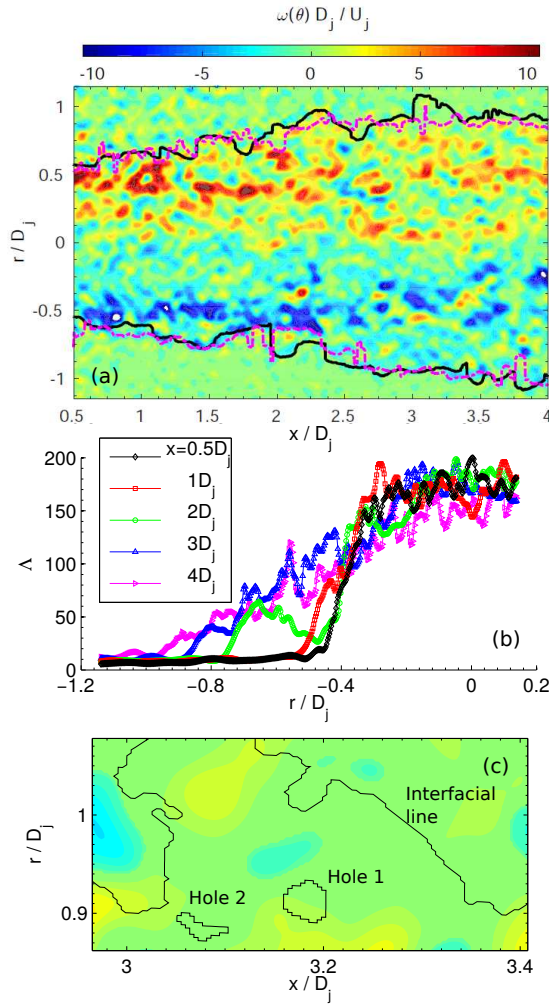
Fig. 20 (a) TNTI based on the scalar interface detected by the proposed method and the velocity criterion marked on an instantaneous vorticity field. Solid line the detected scalar interface (envelop); dashed line interface based on the velocity criterion; (b) the intensity (Λ) distribution across the bottom interface at the indicated downstream distances, after the image denoising; (c) the detected true interfacial lines (not envelop) on top of the vorticity field, with two 'intensity holes' marked.

experiments but is expected to be particularly useful in gas phased experiments where no liquid phased dye can be employed. The vortex ring is an example of unstationary turbulence where strong entrainment and detainment mechanism is involved as a function of time. The near field jet is an example of stationary turbulence, where the flow and the seeding conditions are approximately temporally invariant. The seeding condition is controlled so that the contrast across the scalar interface is large enough to facilitate the interface determination by the very basic wavelet thresholding methods and at the same time it is small enough to allow PIV algorithm to work with negligible extra error after an image local normalisation treatment. The technique is shown to be fairly accurate in both applications. From the
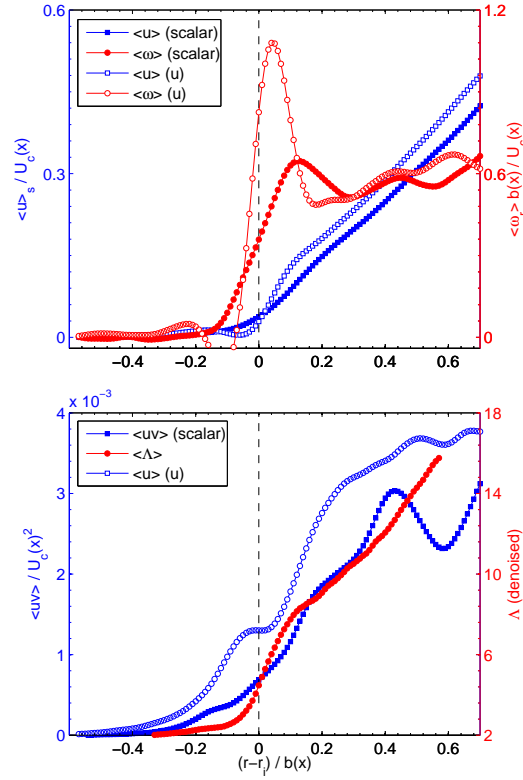
Fig. 21 The ensemble and conditional averaged velocity, vorticity, Reynolds shear stress and concentration profiles near the interface. (a) the velocity and vorticity profiles; (b) the Reynolds shear stress and intensity profiles. The vertical dashed line at $r = r_i$ indicates the interfacial location.

discussions of various physical quantities, the detected scalar interface is shown to make physical sense.

The resolution of the interface is determined by the thickness of the laser sheet and the particle size. First, if the resolution of the scalar concentration is not the main requirement, single pixel resolution is not necessary. Particles seen in the vicinity of the interfacial layer could be randomly distributed within the laser sheet thickness. In a sense this could be advantageous, because it matches the resolution of the PIV measurement in the out-of-plane direction.

Second, for the in-plane component, a particle seen in a camera covers typically 3-4 pixels after the pre-treatment for removing saturated pixels and preventing some undesired effects in PIV processing e.g. peak-locking. This then introduces an uncertainty of about one particle size to the true interface location. Nonetheless, the uncertainty is usually a systematic over-estimation (outside the true interfacial line) of about one particle size. This can be seen in § 4 by analysing synthetic particle images; figure 8 (b). The amount of uncertainty is expected to be more or less equivalent to the camera FOV mis-matching in a careful simultaneous measurement of PLIF and PIV (32, for example) and moreover, this uncertainty is not random but systematic, which means that a compensation can be made in the intensity

threshold selecting stage (figure 5) to shrink the detected interface towards the scalar marked region and to reduce this uncertainty.

One essential condition is the sufficient background particle seeding densities, which is for PIV purposes, while at the same time, the seeding inhomogeneity needs to be massively reduced by an image local normalisation step. To give a quantitative estimation of the working seeding condition range, the averaged pixel intensity ratio across the scalar interface varies from 1.65 (the vortex ring at t2) to 4.6 (the jet). Note that since particles are highly overlapped in the raw image, NPPP is not an accessible quantity. Only after the image local normalisation treatment, NPPP can be estimated. In the current testing cases, the maximum NPPP ratio is shown to be 1.2 for intensity ratio $\Lambda_i/\Lambda_o \approx 4.6$. When this condition is satisfied, the technique is flow independent. This means that it should work for different flow types, or different regions of a given flow.

In addition to the evidence in §4, since scalar interface was used to mark TNTI, indirect comparisons are made by determining various physical quantities associated with the estimated scalar interface. The results show that in both the turbulent vortex ring and the near-field jet, the estimated interface successfully separates the turbulent and the non-turbulent zones, qualitatively agreeing with TNTI criteria based on PLIF information in a previous water based experiment.

References

1. Anand R.K., Boersma B.J., Agrawal A.: Detection of turbulent/non-turbulent interface for an axisymmetric turbulent jet: evaluation of known criteria and proposal of a new criterion. Exp. Fluids 47: 995-1007 (2009)
2. Bisset D.K., Hunt J.C.R., Rogers M.M.: The turbulent/non-turbulent interface bounding a far wake. J. Fluid Mech., 451: 383-410 (2002)
3. Chang S.G., Yu B., Vetterli M.: Spatially adaptive wavelet thresholding with context modeling for image denoising. IEEE *Trans. Image Proc.* 9(9): 1522–1531 (2000)
4. da Silva C.B.: The behaviour of subgrid-scale models near the turbulent/nonturbulent interface in jets. Phys. Fluids, 21(8): 081702 (2009)
5. da Silva C.B., Hunt J.C.R., Eames I., Westerweel J.: Interfacial Layers Between Regions of Different Turbulence Intensity Annu. Rev. Fluid Mech. 46:56790 (2014)
6. Daubechies I.: Ten lectures on wavelets. Philadephia.(1992)
7. Donoho D.L., Johnstone I.M.: Ideal spatial adaptation by wavelet shrinkage. Biometrika. 8: 425–455 (1994)
8. Fukishima C., Aanen L., Westerweel J.: Investigation of the mixing process in an axisymmetric turbulent jet using PIV and LIF. In laser techniques for fluid mechanics (Eds. Adrain RJ, Durao DFG, Durst F, Heitor MV, Maeda M & Whitelaw J.) pp. 339-356. Springer.(2002)
9. Gan L., Nickels T.B.: An experimental study of turbulent vortex rings during their early development. J. Fluid Mech. 649: 467–496 (2010)
10. Gan L., Nickels T.B., Dawson J.R.: An experimental study of a turbulent vortex ring: a three-dimensional respresentation. Exp. Fluids 51(6): 1493–1507 (2011)
11. Gan L., Dawson J.R., Nickels T.B.: On the drag of turbulent vortex rings. J. Fluid Mech. 709: 85–105 (2012)
12. Hinze JO: Turbulence. McGraw-Hill (1975)

13. Hunt J.C.R., Sandham N.D., Vassilicos J.C., Launder B.E., Monkewitz P.A., Hewitt G.F.: Developments in turbulence research: a review based on the 1999 programme of the Issac Newton Institute Cambridge. J. Fluid Mech. 436: 353-391 (2001)
14. Jain A.K.: Fundamentals of digital image processing. Prentice Hall (1989)
15. Jimenez J., Hoyas S., Simens M.P., Mizuno Y.: Turbulent boundary layers and channels at moderate Reynolds numbers. J. Fluid Mech. 657: 335-360 (2010)
16. Keinert F.: Wavelets and multiwavelets. Chapman& Hall/CRC (2004)
17. Khashehchi M., Ooi A., Soria J., Marusic I.: Evolution of the turbulent/non-turbulent interface of an axisymmetric turbulent jet. Exp. Fluids 54:1449–1460 (2013)
18. Corrsin S.: Free-stream boundaries of turbulent flows. NACA Tech. Note, p.1244 (1955)
19. Mallat S.: A theory for multiresolution signal decomposition: the wavelet representation. IEEE *Trans. Pattern Anal. ans Machine Intel.* 11(7): 674–693 (1989)
20. Mallat S.: A wavelet tour of signal processing, the sparse way. Academic press (2009)
21. Mathew J., Basu A.J.: Some characteristics of entrainment at a cylindrical turbulence boundary. Phys. Fluids, 14(7): 2065-2072 (2002)
22. Meyer Y.: Wavelets: Algorithms and applications. SIAM (1993)
23. Vetterli M., Kovacevic J.: Wavelets and subband coding. Prentice Hall (1995)
24. Oppenheim A.V., Schafer R.W., Buck J.R.: Discrete-time signal processing (2nd. edition) Prentice Hall (1999)
25. Prasad R.R., Sreenivasan K.R.: Scalar interfaces in digital images of turbulent flows. Exp. Fluids 7:259–264 (1989)
26. Pfadler S., Beyrau F., Leipertz A.: Flame front detection and characterization using conditioned particle image velocimetry (CPIV) Optics Express 15(23):15444-15456 (2007)
27. Semin N., Elsinga G., Westerweel J.: Detection of the laminar superlayer from tpiv measurements in a turbulent jet. Seventh International Symposium on tuebulent and shear flow phenomena (TSFP-7) (2011)
28. Townsend A.A.: The structure of turbulent shear flows. Cambridge University Press (1976)
29. Umbaugh S.E.: Computer vision and image processing. Prentice Hall (1998)
30. Westerweel J., Hofmann T., Fukushima C., Hunt J.C.R.: The turbulent/non-turbulent interface at the outer boundary of a self-similar turbulent jet. Exp. Fluids 33:873–878 (2002)
31. Westerweel J., Fukushima C., Pedersen J.M., Hunt J.C.R.: Mechanics of the turbulent/nonturbulent interface of a jet. Phys. Rev. Lett. 95:174501 (2005)
32. Westerweel J., Fukushima C., Pedersen J.M., Hunt J.C.R.: Momentum and scalar transport at the turbulent/non-turbulent interface of a jet. J. Fluid Mech. 631:199-230 (2009)
33. Willert C.: Stereoscopic digital particle image velocimetry for application in wind tunnel flows. Meas. Sci. Technol. 8:1465–1479 (1997)
34. Yang R., Yin L., Gabbouj M., Astola J., Neuvo Y.: Optimal weighted median filters under structural constraints. IEEE Trans. Signal Processing, 43:591-604 (1995)